Cryo-electron microscopy structure and potential enzymatic function of human six-transmembrane epithelial antigen of the prostate 1 (STEAP1)

Wout Oosterheert*[ID] and Piet Gros*[ID]

From the Crystal and Structural Chemistry, Bijvoet Centre for Biomolecular Research, Department of Chemistry, Faculty of Science, Utrecht University, Utrecht, The Netherlands

Edited by Peter Cresswell

Six-transmembrane epithelial antigen of the prostate 1 (STEAP1) is an integral membrane protein that is highly up-regulated on the cell surface of several human cancers, making it a promising therapeutic target to manage these diseases. It shares sequence homology with three enzymes (STEAP2–STEAP4) that catalyze the NADPH-dependent reduction of iron(III). However, STEAP1 lacks an intracellular NADPH-binding domain and does not exhibit cellular ferric reductase activity. Thus, both the molecular function of STEAP1 and its role in cancer progression remain elusive. Here, we present a ~3.0-Å cryo-EM structure of trimeric human STEAP1 bound to three antigen-binding fragments (Fabs) of the clinically used antibody mAb120.545. The structure revealed that STEAP1 adopts a reductase-like conformation and interacts with the Fabs through its extracellular helices. Enzymatic assays in human cells revealed that STEAP1 promotes iron(III) reduction when fused to the intracellular NADPH-binding domain of its family member STEAP4, suggesting that STEAP1 functions as a ferric reductase in STEAP heterotrimers. Our work provides a foundation for deciphering the molecular mechanisms of STEAP1 and may be useful in the design of new therapeutic strategies to target STEAP1 in cancer.

Since its discovery in 1999 as a multispan membrane protein highly expressed on prostate cancer cells (1), six-transmembrane epithelial antigen of the prostate 1 (STEAP1) emerged as a cancer antigen expressed in various human cancers, including prostate, bladder, colorectal, lung, ovarian, and breast carcinoma and Ewing sarcoma. Because its expression in physiological tissues is minimal and mainly confined to the prostate gland (2), STEAP1 represents a potentially attractive therapeutic tool as both a cancer biomarker and a target for anticancer therapies (2–4). Indeed, several strategies for targeting STEAP1 in cancer have been explored; in 2007, a study reported the production and characterization of two monoclonal antibodies (mAb120.545 and mAb92.30) that bind STEAP1 with nanomolar affinity on prostate cancer cells and inhibit the growth of prostate and bladder tumor xenografts in mice (5). More recently, clinical studies employing humanized variants of mAb120.545 that target

STEAP1 were conducted, including 1) a phase I trial using an antibody-drug conjugate (termed DSTP3086S or Vandortuzumab Vedotin) to target prostate cancer (6–8) and 2) a combined phase I/phase II trial for the PET imaging of metastatic castration-resistant prostate cancer using Zr^{89}-labelled antibody (termed [^{89}Zr]Zr-DFO-MSTP2109A) (9–11). Besides antibody-based strategies, several *in vitro* and *in vivo* studies revealed that STEAP1-derived peptides are immunogenic and thus suitable for recognition by cytotoxic T lymphocytes (12–16), indicating that STEAP1 could represent a potential candidate for the development of anticancer vaccines (4, 17).

STEAP1 belongs to a protein family that comprises three metalloreductases (18, 19), STEAP2–STEAP4, also known as STAMP1–STAMP3 (20–22), which reduce iron(III) and copper(II) and are also associated with cancer progression (23–25). At the molecular level, the four STEAP proteins are predicted to adopt a common architecture with intracellular N and C termini, six transmembrane helices, and a single heme B prosthetic group bound in the transmembrane domain (TMD) (26). STEAP2–STEAP4 also contain an intracellular oxidoreductase domain (OxRD) that binds NADPH (27, 28). The ferric and cupric reductase mechanism of STEAP2–STEAP4 is defined by electron transfer from intracellular NADPH through membrane-embedded FAD and heme cofactors to chelated metal-ion complexes at the membrane extracellular side (26, 29). In contrast to STEAP2–STEAP4, STEAP1 does not exhibit metalloreductase activity when overexpressed on mammalian cells (19), suggesting that it may have a distinct yet unidentified function. However, a recent study revealed that dithionite-reduced, purified STEAP1 retains heme and is capable of reducing metal-ion complexes and oxygen (30), indicating that the absence of a binding site for an electron-donating substrate like NADPH could explain the lack of reductase activity for STEAP1. It has been proposed that STEAP1 may have a functional role in heterooligomeric complexes with other STEAP paralogues (19, 30). In support of this, its expression often correlates with the expression of STEAP2 in cancers (17) and both proteins co-purify in detergent (30), suggesting that they could form a functional complex. Further indications for a functional heterotrimeric STEAP complex emerged from the recent cryo-EM structures of homotrimeric human STEAP4 (29), which revealed a domain-swapped architecture, with the intracellular OxRD positioned beneath the TMD of the adjacent protomer. This arrangement supports a model in which the heme in

---

* For correspondence: Wout Oosterheert, w.oosterheert@uu.nl; Piet Gros, p.gros@uu.nl.
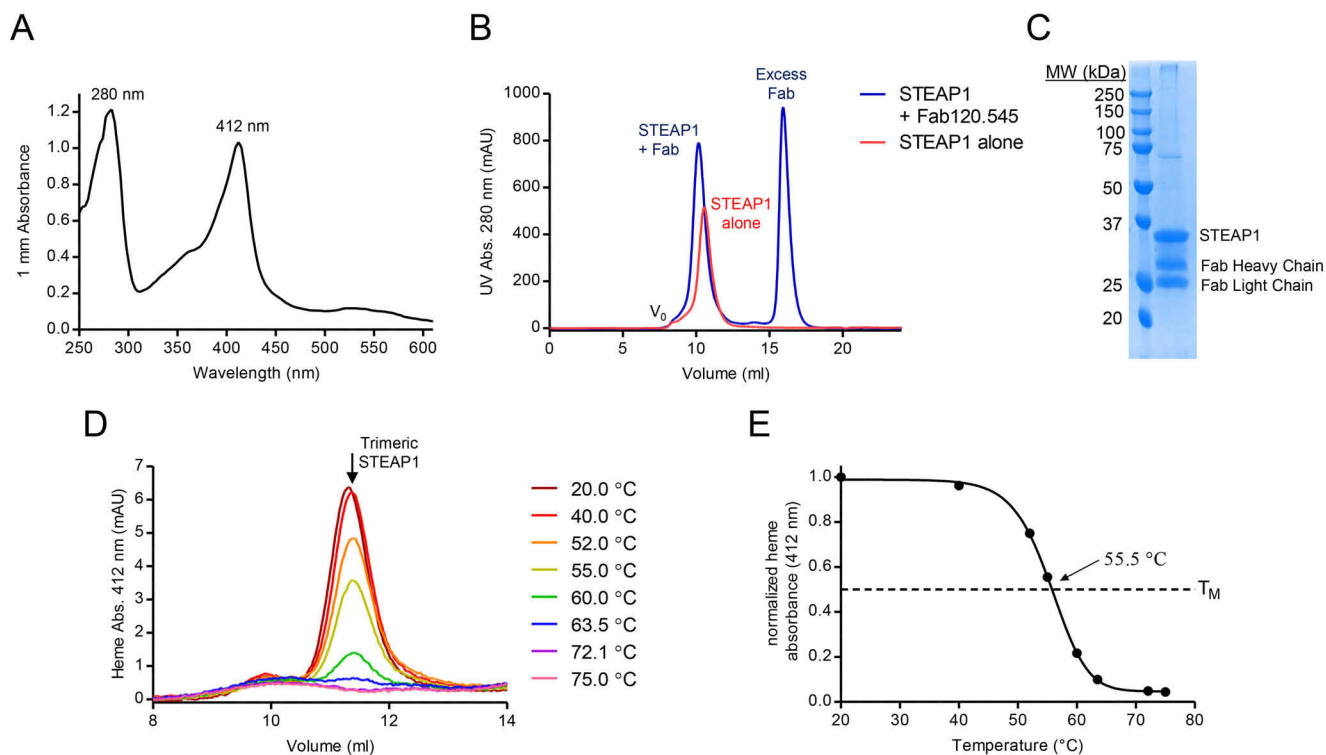
Figure 1. STEAP1 purification and stability. *A*, UV-visible spectrum of the purified STEAP1-Fab120.545 complex used for EM sample preparation. The protein and heme absorbance peaks exhibit maxima at 280 and 412 nm, respectively. *B*, size-exclusion chromatography elution profile of STEAP1 in the absence (*red*) or presence (*blue*) of excess Fab120.545. Fractions collected from the STEAP1-Fab120.545 sample were used for EM sample preparation. *C*, SDS-PAGE of the purified STEAP1-Fab120.545 complex. *D*, heme absorbance size-exclusion chromatography elution profiles of STEAP1 after 10 min of incubation at several temperatures. *E*, melting curve for digitonin-purified STEAP1, generated by using the peak maxima from *D*. STEAP1 exhibits a melting temperature of 55.5 °C.

STEAP1 receives electrons from NADPH bound to an adjacent STEAP2/3/4 subunit. However, the *in vivo* redox activity of STEAP1, in both the absence and presence of other STEAP paralogues, remains to be established. In addition, there are no high-resolution structures available to help distinguish a functional role for STEAP1 as a metalloreductase or, as previously proposed, a potential channel or transporter protein (1, 2, 5, 31). Thus, although STEAP1 is a populous plasma membrane component of many different types of cancer cells and hence is a promising novel therapeutic target, its structure and function in both health and disease remain unknown.

Here, we present the cryo-EM structure of full-length, trimeric human STEAP1 bound to three Fab fragments of the therapeutically relevant mAb120.545. The Fabs dock on the extracellular helices of STEAP1 through an extensive polar interface. The TMD of STEAP1 resembles the architecture of the STEAP4 TMD and exhibits cellular ferric reductase activity when fused to the NADPH-binding OxRD of STEAP4.

Results

Biochemical characterization of STEAP1

A previous pioneering study reported the biophysical and electrochemical characterization of N-terminally truncated rabbit STEAP1, purified from insect cells in lauryl maltose neopentyl glycol detergent (30). Our initial attempts to purify full-length, human STEAP1 from mammalian HEK cells using a similar protocol were hampered by the loss of the noncovalently bound heme B cofactor during the purification, suggest-

ing that STEAP1 was not natively folded. Therefore, we screened several other detergents for the solubilization of STEAP1 and identified digitonin as a suitable replacement for lauryl maltose neopentyl glycol. In digitonin, the purified protein retained its heme cofactor (Fig. 1A) and eluted as a monodisperse peak in size-exclusion chromatography experiments (Fig. 1, B and D). In addition, thermostability assays revealed a melting temperature of ∼55.5 °C for STEAP1 in digitonin (Fig. 1, D and E), indicating that the protein was stable outside its native membrane environment. To assess whether the extracellular domains of purified STEAP1 adopted a conformation similar to those of membrane-embedded STEAP1, we tested the binding of STEAP1 to the Fab fragment of mAb120.545, which exhibits 1 nM affinity for STEAP1 on cells (5) and recognizes a conformation-dependent, nonlinear epitope (32). Size-exclusion chromatography assays revealed a smaller elution volume for STEAP1 when it was premixed with Fab120.545 (Fig. 1B), suggesting the formation of a complex, which was then confirmed by SDS-PAGE analysis of the eluted sample (Fig. 1C). Thus, the conformation of the STEAP1 epitope recognized by the Fab fragment on cells is preserved during the detergent solubilization and purification of STEAP1.

Cryo-EM structure determination

To gain insights into the molecular architecture of STEAP1, we set out to obtain a structural model of the protein using single-particle cryo-EM. Full-length, trimeric STEAP1 proved to be a challenging sample for EM due to its small size (<120 kDa)
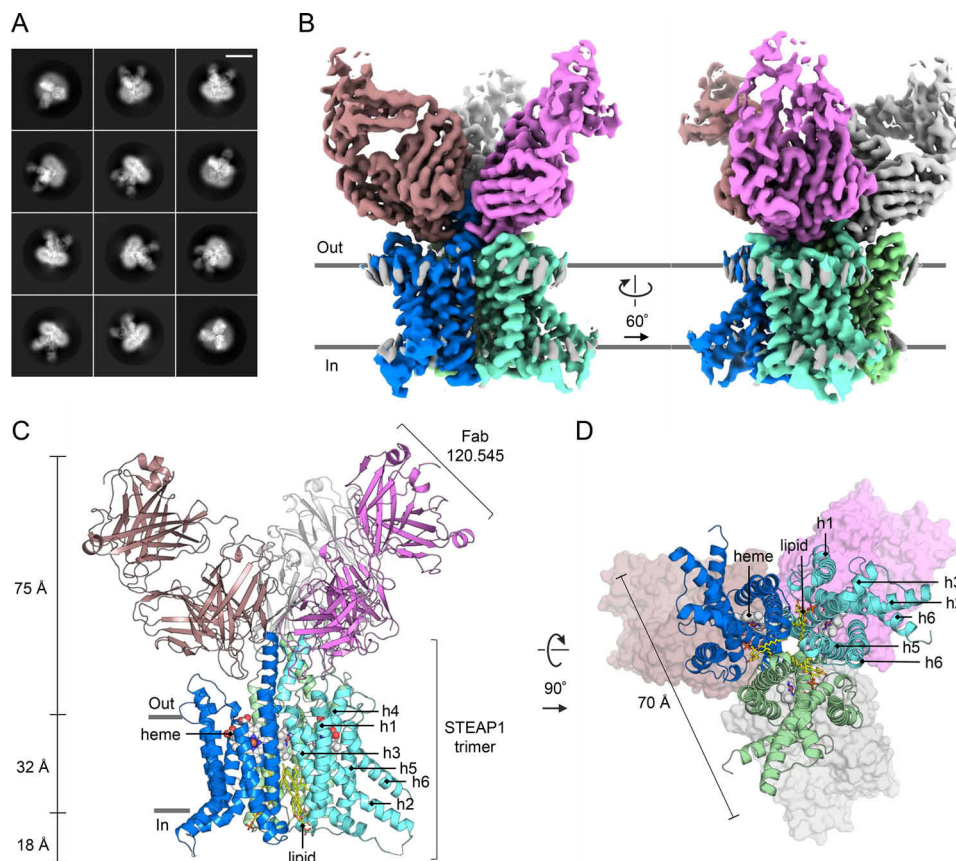
Figure 2. Cryo-EM structure of the STEAP1-Fab120.545 complex. *A*, exemplary 2D class averages. The box size corresponds to 300 × 300 pixels (309 × 309 Å). The length of the *scale bar* in the top right corner is 100 Å. More 2D class averages are shown in Fig. S2*B*. *B*, two orientations of the unsharpened cryo-EM density map at 3.0-Å resolution. The STEAP1 chains are colored *blue, cyan* and *green*; and the Fab molecules are colored *brown, magenta* and *light-gray*. *C* and *D*, atomic model of the STEAP1-Fab120.545 complex as viewed parallel to the membrane as a side view (*C*) or orthogonal to the membrane from the cytoplasmic side (*D*). In *D*, the Fabs are shown as surfaces.

and the absence of folded domains protruding from the membrane region. To create a larger particle with more extramembrane features to facilitate EM image processing, we opted to determine the structure of STEAP1 purified in complex with Fab120.545. The complementarity-determining regions of Fab120.545 are identical to those present in STEAP1 antibodies used in clinical trials (Fig. S1), indicating that the structure of the STEAP1-Fab120.545 complex could also be useful in engineering antibodies and other molecules that target STEAP1 in cancer. Micrographs collected on a 200-kV Talos Arctica microscope showed nonaggregated particles distributed in vitreous ice (Fig. S2*A*). Subsequent 2D classification experiments yielded class averages with clear secondary structure elements and furthermore revealed that more than one Fab fragment is bound to micelle-embedded STEAP1 (Fig. 2*A*; Fig. S2*B*). Image processing in RELION (33) finally resulted in a reconstructed cryo-EM-density map at ~3.0-Å resolution (Fig. 2*B*; Fig. S2, *C–F*). The map displayed well-defined side chain density for the TMD of STEAP1 and the variable regions of the Fab (Fig. S3). The model for STEAP1 was built with the TMD of STEAP4 as the template (29) (PDB code 6HCY), whereas the starting model for the Fab was generated through the PIGS homology server (34). The refined structure has acceptable stereochemistry and exhibits high correlation to the cryo-EM density map within the determined resolution (Fig. S3, *G* and *H*; Table 1).

Architecture

The cryo-EM structure reveals a 1:1 stoichiometry of the STEAP1-Fab120.545 complex, with 3 STEAP1 protomers interacting with 3 Fab molecules (Fig. 2, *B–D*). The Fabs bind at the extracellular region of STEAP1, consistent with the observation that the antibody targets STEAP1 expressed on intact cancer cells. The intracellular loops of STEAP1 extend ~18 Å from the membrane region into the cytoplasm, whereas the Fabs protrude up to ~75 Å into the extracellular space. STEAP1 adopts a trimeric arrangement that is similar to that of its family member STEAP4 (41% amino acid sequence identity; root mean square deviation (RMSD) of 0.8 Å for 640 Cα atoms) (Fig. 3). Each STEAP1 subunit contains six membrane-spanning α-helices (h1–h6) that define the TMD of the protein. A single B-type heme cofactor is surrounded by helices, h2, h3, h4, and h5 at the extracellular membrane leaflet (Fig. S3*B*). Strictly conserved histidine residues H175 and H268 coordinate the central iron moiety of the heme prosthetic group, thereby resembling the hexacoordinated heme arrangement of STEAP4. At the intracellular membrane leaflet side of the TMD, we observed weak density not corresponding to any protein residues. An overlay with the structure of STEAP4 revealed that the observed density overlaps with the flavin ring of the FAD-binding site in STEAP4 (Fig. S3*D*). The FAD-interacting

residues in the TMD of STEAP3 and 4 are conserved in STEAP1, and the STEAP1-Fab120.545 cryo-EM sample was supplemented with 1 mM FAD before grid freezing. However, STEAP3 and STEAP4 also interact with the adenine moiety of FAD via their intracellular OxRD (26, 29) (Fig. 3*B*; Fig. S3*D*), which is missing in STEAP1. In line with this, STEAP3 and STEAP4 exhibit a low micromolar affinity for FAD ($K_d = \sim 1$ μM) (26, 29), whereas the affinity of STEAP1 for FAD is much weaker ($K_d = 34$ μM) (30). The cryo-EM density in this region could therefore correspond to a loosely bound FAD cofactor, although the weak density does not allow for modelling of the complete cofactor. Instead of an OxRD of $\sim$175 amino acids in length, STEAP1 contains a 69-residue N-terminal intracellular tail with no predicted domain architecture. Indeed, we observed no density for the first 65 intracellular amino acids of STEAP1, indicating that these residues are flexible, which is consistent with *in silico* disorder predictions using RONN (35). Thus, in contrast to other STEAP family members, the homotrimeric human STEAP1 structure does not harbor a folded N-terminal intracellular domain.

STEAP1-Fab120.545 interface

We next analyzed the interface between STEAP1 and Fab120.545. The epitope recognized by the Fab spans the first and second extracellular regions (EC1 and EC2, respectively) of STEAP1, which bridge membrane helices h1–h2 and h3–h4. The total interface formed between the STEAP1 trimer and three Fabs comprises $\sim$5,730 Å^2 of buried surface area and is arranged so that a single Fab molecule interacts with all three STEAP1 protomers. The interface is stabilized by a network of polar and hydrophobic interactions and can largely be described by two "interaction hot spots" on the EC2 of STEAP1 (Fig. 4, *A* and *B*). The first hot spot involves the extracellular helix of STEAP1 (residues 186–201), which extends from membrane helix h3. Y190, N194, W195, and Q198 interact with Fab heavy and light chain residues $Y102_H$, $Y104_H$, $Y108_H$, $Y31_L$, and $S33_L$ (Fab chain identifier in subscript) (Fig. 4*A*). The carbonyl group of $S33_L$ forms a hydrogen bond with the side chain of Y107 of the EC1, whereas $Y104_H$ bridges two STEAP1 protomers by interacting with both Y190 and W195 from different chains. The second hot spot involves residues Q201, Q202, N203, Q205, and D206, which reside in the loop that connects the extracellular helix of STEAP1 to membrane helix h4. Hot spot 2 consists of numerous polar interactions, including a salt bridge between D206 and $R32_L$. Other Fab residues involved in binding to hot spot 2 are $Y51_H$, $S57_H$, $T58_H$, $S59_H$, $Q27_L$, $S33_L$, $N99_L$, and $Y100_L$ (Fig. 4*B*). Besides the Fab residues in close proximity (<4 Å) to STEAP1, we identified three aspartate residues ($D103_H$, $D105_H$, and $D106_H$) in the Fab heavy chain that are oriented toward the basic amino acid ring above the heme (Fig. 4*C*). These aspartates are at least 4.5 Å separated from any STEAP1 residues and could participate in long-range electrostatic interactions with the basic ring of STEAP1. Interestingly, in STEAP4, the corresponding basic amino acids constitute the substrate-binding site (Fig. 4*D*). To experimentally verify the STEAP1-Fab interface observed in the structure, we generated several mutants of Fab120.545 and tested their ability to bind

Table 1

Cryo-EM data collection, refinement, and validation statistics for STEAP1-Fab120.545 (PDB code 6Y9B, EMDB-10735)

Data collection and processing	
Microscope	Talos Arctica
Camera	Gatan K2 Summit + GIF filter
Magnification	$\times$130,000
Voltage (kV)	200
Frame/total exposure time (s)	0.25/6.5
No. of frames	26
Electron exposure (e$^-$/Å^2)	49.5
Defocus range (μm)	-0.5 to -3.0
Pixel size (Å)	1.029
Symmetry imposed	C3
No. of micrographs	5,325
No. of initial particle images	616,302
No. of final particles images	169,426
Map resolution (FSC = 0.143 threshold) (Å)	2.97
Map resolution range (Å)	2.9–5.0
Refinement	
Model resolution (FSC = 0.5 threshold) (Å)	3.04
Map sharpening B factor (Å^2)	0
Model composition	
No. of nonhydrogen atoms	11,889
No. of protein residues	1,434
No. of ligands	6
B-factors (Å^2)	
Protein	100.5
Ligands	92.8
RMSD	
Bond lengths (Å)	0.004
Bond angles (°)	0.536
Validation	
MolProbity score	1.69
Clash score	5.08
Poor rotamers (%)	1.2
Ramachandran plot	
Favored (%)	94.6
Allowed (%)	5.4
Disallowed (%)	0

purified STEAP1 by using size-exclusion chromatography assays (Fig. S4). Mutants $R32_LE$ and $N99_LD$ were designed to create charge repulsions in hot spot 2 between STEAP1 and Fab120.545. As expected, we did not observe binding events for these two mutants (Fig. S4, *A*–*C*). Fab mutants $D103_HN$, $D105_HN$,$D106_HN$ (Fab-NNN) and $D103_HA$,$D105_HA$,$D106_HA$ (Fab-AAA) similarly did not interact with purified STEAP1 (Fig. S4, *A*, *D*, and *E*), indicating that the long-range electrostatic interactions between the three Fab aspartates and STEAP1 are essential for maintaining a high-affinity antibody-antigen complex.

Generation of a functional STEAP4/1 fusion protein

The reductase-like architecture of STEAP1 (Fig. 3) and its heme redox potential of -114 to -118 mV (30) indicate that the protein could be functional in reducing metal-ion complexes *in vivo*. To the best of our knowledge, however, there are currently no experimental data available that show that STEAP1 is capable of reducing ferric iron in a physiological setting. Although STEAP1 may form relevant heterotrimeric complexes with other STEAP homologs (30), coexpressions of different STEAP family members will likely result in a mixed population of homo- and heterotrimers, making cellular ferric reductase experiments difficult to interpret. To overcome these hurdles and to assess whether the TMD of STEAP1 could direct electron transport across mammalian cell membranes, we aimed to design a construct in which the STEAP1 TMD was
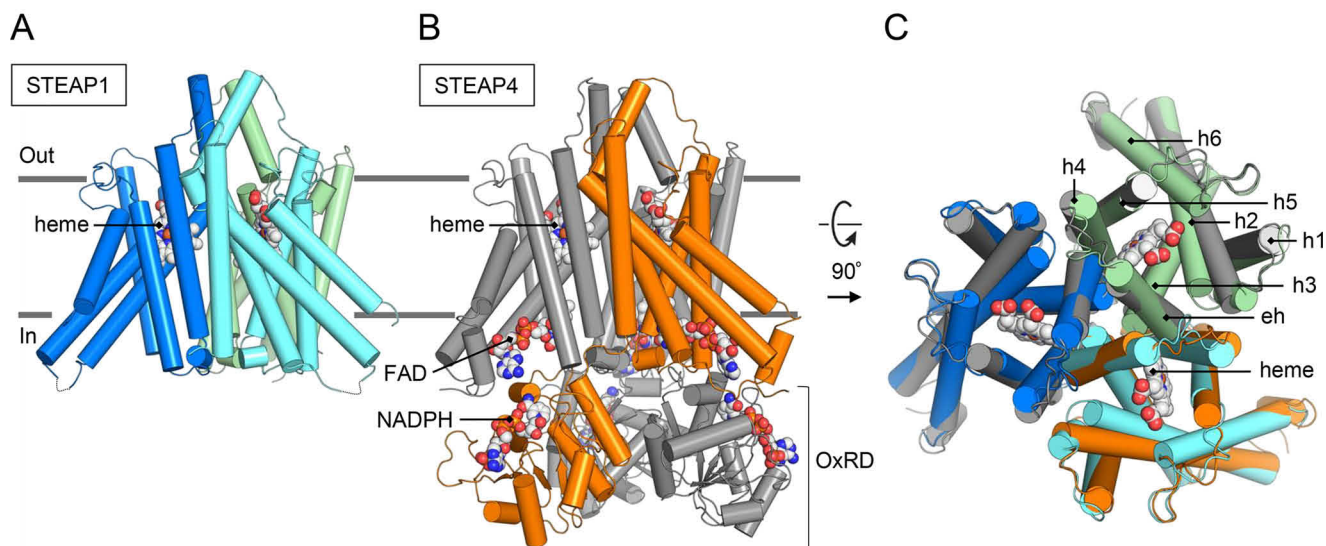
Figure 3. Structural similarities between human STEAP1 and STEAP4. *A* and *B*, aligned models (RMSD of 0.8 Å for 640 Cα atoms) of STEAP1 (*A*) and STEAP4 (*B*) shown parallel to the membrane. The STEAP1 chains are colored *blue*, *cyan* and *green*. For STEAP4, one chain is colored *orange* and two chains are depicted in *gray*. *C*, overlay of STEAP1 and the TMD of STEAP4 (residues 195–454) shown orthogonal to the membrane from the extracellular side. Overlapping membrane helices are annotated.

fused to the intracellular OxRD of another STEAP homologue. To this end, a sequence alignment of all human STEAP proteins revealed that STEAP4 and STEAP1 share a common three-amino acid LFP motif at the start of membrane helix h1. Additionally, an overlay of their cryo-EM structures did not show any obvious clashes between the OxRD of STEAP4 and the TMD of STEAP1. Thus, we generated a construct that spans residues M1–Q195 of STEAP4, the shared LFP motif, and residues Q69–L339 of STEAP1, which we termed STEAP4/1$_{chimera}$ (Fig. 5, *A and B*). We then expressed STEAP4/1$_{chimera}$ in HEK293 cells and compared its cellular reductase activity to cells expressing STEAP1 or STEAP4, using the physiologically relevant ferric citrate as a substrate. Consistent with a previous study (19), overexpression of STEAP1 did not result in measurable cell-surface ferric reductase activity, compared with the empty-vector control, whereas cells expressing STEAP4 reduced ~57 pmol Fe^{3+}/min/well (Fig. 5*C*). Intriguingly, the STEAP4/1$_{chimera}$-expressing cells also showed highly significant reductase activity of ~43 pmol Fe^{3+}/min/well (Fig. 5*C*). To verify that the observed activity depended on transmembrane electron transport through the TMD of STEAP1, we additionally tested STEAP4/1$_{chimera}$ mutants R161E and H175A (STEAP1 numbering) in which the FAD and heme-binding sites in the TMD, respectively, are abolished. Cells expressing STEAP4/1$_{chimera}$-R161E and STEAP4/1$_{chimera}$-H175A did not exhibit any ferric reductase activity (Fig. 5*C*), indicating that the STEAP1 TMD of the chimera is indeed crucial for cell-surface iron reduction. Confocal microscopy experiments subsequently confirmed that all expressed proteins except for STEAP4/1$_{chimera}$-H175A localized to the plasma membrane (Fig. S5). Taken together, our cell-based experiments reveal that STEAP1 adopts a conformation that facilitates transmembrane electron transport to reduce ferric citrate at the membrane extracellular side. Therefore, the lack of reductase activity of the protein can be explained by the ab-

sence of a binding site for an electron-donating substrate in homotrimeric STEAP1.

Fab120.545 inhibits ferric reductase activity of STEAP4/1$_{chimera}$

Because Fab120.545 binds close to the putative substrate-binding site in STEAP1 (Fig. 4, *C and D*), we assessed whether Fab binding could influence the ferric reductase activity of STEAP4/1$_{chimera}$. Indeed, the addition of 4 μM Fab120.545 to cells expressing STEAP4/1$_{chimera}$ led to a significant decrease in iron citrate reduction, from ~43 to ~18 pmol Fe^{3+}/min/well (Fig. 5*C*). Conversely, the activity of STEAP4 was unchanged, indicating that the Fab specifically recognizes an extracellular epitope of STEAP1. We further characterized the inhibitory properties of the Fab by incubating cells expressing STEAP4 or STEAP4/1$_{chimera}$ with different Fab concentrations. This revealed a Fab-concentration-dependent effect on the inhibition of the ferric reductase activity of STEAP4/1$_{chimera}$, while the amount of iron(III) reduced by STEAP4 remained unaltered over the entire concentration range tested (Fig. 5*D*).

Discussion

Based on its amino acid sequence and subcellular localization, STEAP1 was previously predicted to function as a channel or transporter protein (1, 2, 5, 31). The cryo-EM structure of STEAP1 bound to antibody fragment Fab120.545 revealed a trimeric arrangement similar to that of its family member STEAP4 (Fig. 3), showing no obvious structural features of ion channels or transporters. Instead, the strictly conserved FAD-binding residues and putative loosely bound FAD at the inner-membrane leaflet of the TMD (Fig. S3*D*), the heme-binding site at the outer-membrane leaflet (Fig. S3*B*), and the basic amino acid ring above the heme (Fig. 4*C*) all imply that STEAP1 may function as a transmembrane oxidoreductase. In our previous
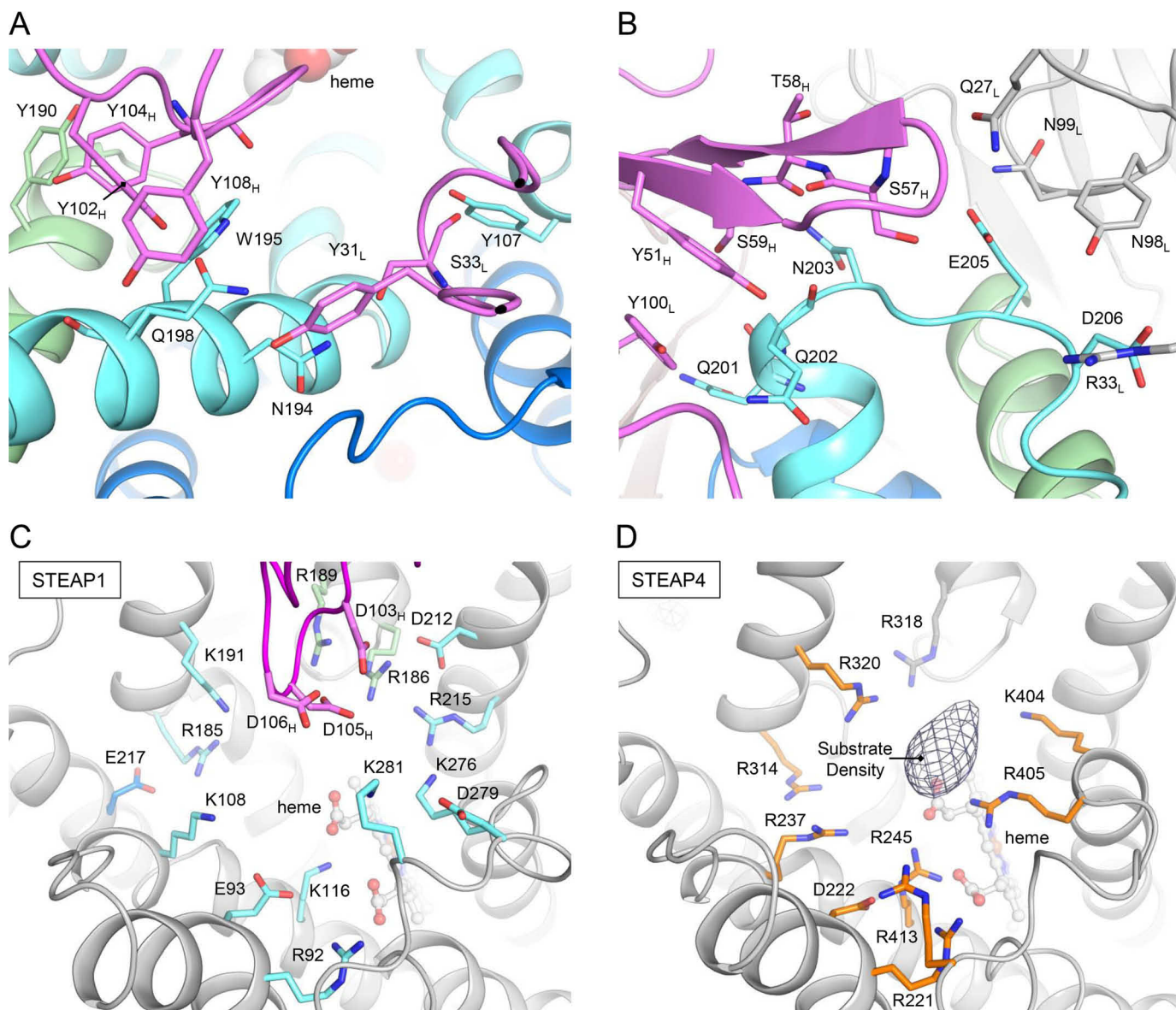
Figure 4. Fab120.545 binding at the putative substrate-binding site. *A* and *B*, interactions between STEAP1 and Fab120.545 at hot spot 1 (*A*), corresponding to the extracellular helix of STEAP1, and hot spot 2 (*B*), the loop between the extracellular helix and membrane helix h4. Amino acid backbones are shown as sticks only when they contribute to the interface. The STEAP1 chains are colored *blue*, *cyan* and *green*; and the Fab molecules are colored *magenta* and *light-gray*. *C*, amino acid environment above the heme in the STEAP1-Fab structure. All charged residues are shown as sticks. The Fab light chain is omitted from the figure for clarity. STEAP1 helices are colored *gray* for clarity. STEAP1 residues are colored by chain in *cyan* or *green*. Fab heavy chain residues are colored *magenta*. *D*, amino acid environment above the heme in the STEAP4 structure (PDB code 6HCY, EMDB-0199). All charged residues are shown as sticks. The difference density (taken from EMDB-0199) that corresponds to substrate Fe(III)-nitrilotriacetic acid is depicted in mesh. STEAP4 residues are colored by chain in *orange* or *gray*.

work, we showed that substrate iron(III), complexed to a negatively charged chelator like citrate, binds in the basic ring of STEAP4 (Fig. 4D) and we proposed that this ring of positive amino acids may polarize the iron(III)-chelator complex to facilitate the iron reduction reaction (29). The presence of a comparable positively charged ring (Fig. 4, *C* and *D*) indicates that STEAP1 harbors a similar protein environment for the reduction of iron(III).

We investigated whether the TMD of STEAP1 is capable of directing transmembrane electron transport by generating a fusion construct between the intracellular region of STEAP4 and the TMD of STEAP1, termed STEAP4/1$_{chimera}$ (Fig. 5, *A* and *B*). Cell-surface-expressed STEAP4/1$_{chimera}$ catalyzed the

reduction of iron citrate, providing evidence that STEAP1 is a functional reductase, albeit only when a binding site for the intracellular electron-donating substrate NADPH is available (Fig. 5, *C* and *D*). The lack of enzymatic activity of STEAP4/1$_{chimera}$-R161E (Fig. 5C), which localizes to the plasma membrane in HEK cells (Fig. S5D), confirmed that the TMD of STEAP1 enables transmembrane electron transport. We also showed that STEAP4/1$_{chimera}$-H175A exhibited no significant ferric reductase activity (Fig. 5C). However, fluorescence microscopy experiments revealed that this mutant resides almost exclusively in intracellular compartments (Fig. S5E), suggesting that the protein misfolds when the heme cofactor-binding site is abolished.
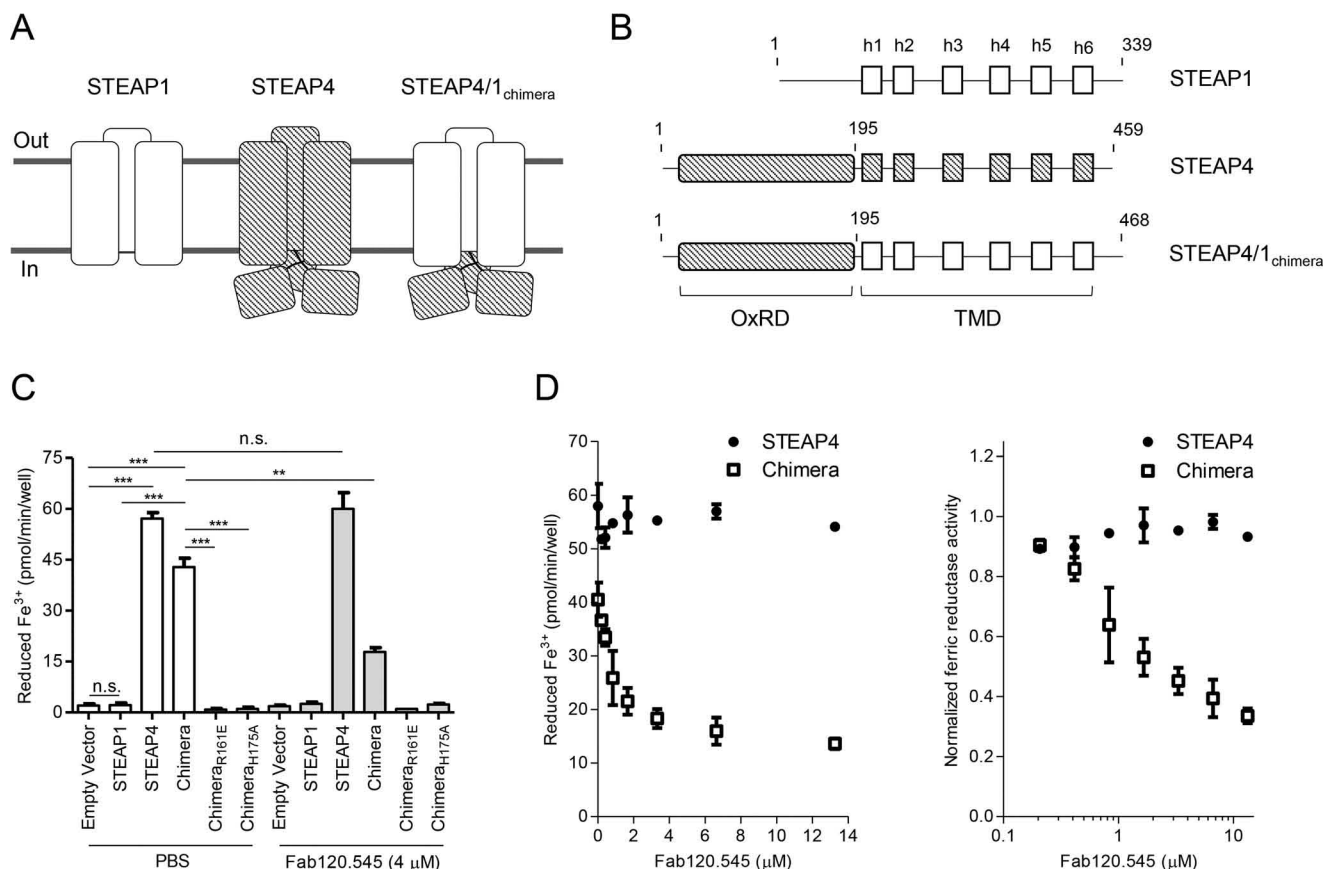
Figure 5. Cellular ferric reductase activity of STEAP protein variants. *A*, schematic topological representation of naturally occurring STEAP1 and STEAP4 and the designed fusion protein STEAP4/1chimera. Domains of STEAP1 are shown in *solid white*, whereas STEAP4 domains are depicted in *diagonal stripes*. *B*, domain composition of STEAP1, STEAP4, and STEAP4/1chimera constructs used for cellular ferric reductase experiments. *C*, cell-surface ferric reductase activity of STEAP protein variants supplemented with PBS or with 4 μM Fab120.545. The experiment was performed in triplicate, and *error bars* represent the S.D. *D*, cell-surface ferric reductase activity of STEAP4 and STEAP4/1chimera with different concentrations of added Fab120.545. *Error bars* represent the S.D. from triplicate experiments. The *right panel* shows the same data normalized to an activity of 1 at 0 μM Fab120.545, with a logarithmic x axis.

The addition of Fab120.545 resulted in a concentration-dependent decrease of ferric reductase activity of STEAP4/1chimera-expressing cells but not of STEAP4-expressing-cells (Fig. 5, *C and D*). This demonstrates that the Fab likely does not interact with STEAP4, which can be explained by the observation that the glycan on STEAP4 residue N323 would clash with the Fab light chain. In contrast, the residue at the equivalent position in STEAP1 (N194) is not glycosylated and forms a hydrogen bond with S33$_L$ (Fig. 4*A*).

How does Fab120.545 inhibit the cell-surface ferric reductase activity of STEAP4/1chimera? The conformations of the extracellular regions of STEAP4 and Fab-bound STEAP1 are similar (Fig. 3); therefore, the binding of Fab120.545 is not expected to induce large conformational changes in STEAP1. Instead, the Fab partially blocks access to the putative substrate-binding site in the basic ring above the heme (Fig. 4*C*). Alternatively, Fab residues D103$_H$, D105$_H$, and D106$_H$ might neutralize the positively charged substrate-binding site and thereby prevent substrate polarization. However, mutagenesis of these aspartates to either asparagines (Fab-NNN) or alanines (Fab-AAA) resulted in a loss of binding of Fab120.545 to purified STEAP1 (Fig. S4, *A, D, and E*), and thus this hypothesis could not be tested. Nevertheless, our results suggest that antibodies can be employed as tools to inhibit the ferric reductase activity of

STEAP enzymes. Additionally, the 3:3 STEAP1/Fab120.545 stoichiometry (Fig. 2, *B* and *C*) indicates that full-length antibodies may cross-link STEAP1 trimers into higher-order assemblies on cell membranes. A similar antibody-induced cross-linking mechanism has recently been reported for the therapeutic antibody rituximab binding to its dimeric target protein CD20 (36).

In conclusion, the study presented here describes the first structure-function analysis of the human cancer antigen STEAP1. Our results support a model in which STEAP1 forms heteromeric assemblies with partner proteins that recruit and orient intracellular electron-donating substrates toward the TMD of STEAP1, enabling transmembrane electron transport and the reduction of extracellular metal-ion complexes. This model warrants further investigations into the physiological function of STEAP1; for example, the incorporation of STEAP1 into STEAP heterotrimers might moderate iron(III) reduction rates locally and thereby prevent deleterious reactions associated with iron overload. Therefore, we envision that it will be of great interest to focus future research endeavors on these putative assemblies of STEAP1 with STEAP2–STEAP4 family members and other unidentified accessory proteins in relevant cancer tissues. Ultimately, understanding the molecular principles that underly the function of STEAP1 will guide the design of anti-STEAP1-

Experimental procedures

Chemicals

All chemicals were purchased from Sigma-Aldrich unless specified otherwise.

Constructs

Codon-optimized DNA coding for human STEAP1 (Uni-ProtKB code Q9UHE8) and STEAP4 (UniProtKB code Q687X5) for mammalian cell expression was purchased from GeneArt. The full-length STEAP1 construct used for structure determination was cloned in a pUPE expression vector (U-Protein Express BV) with a C-terminal Strep-tag. The STEAP4/1$_{chimera}$ construct was generated through Gibson assembly cloning (NEB). For functional assays in HEK cells, all constructs were cloned in a pUPE expression vector with a C-terminal GFP-Strep-tag with a tobacco etch virus protease site. Mutagenesis of STEAP constructs was performed using the Q5 site-directed mutagenesis kit (NEB). The primers used in this study are listed in Table S1. The amino acid numbering of STEAP1 was used for mutations introduced in the STEAP4/1$_{chimera}$ (R161E and H175A) because the mutated amino acids reside in the STEAP1 domain of the chimera. These residues correspond to R290 and H304 in both STEAP4/1$_{chimera}$ and STEAP4. All Fab120.545 variants were a kind gift from Genmab BV and were produced at our request.

Protein expression and purification for cryo-EM

The protein production protocol was adapted from the previously described protocol for STEAP4 (29). Full-length STEAP1 with a C-terminal Strep-tag was expressed in HEK293 GnTI⁻ suspension cells (provided by U-Protein Express BV). Cells were grown at 37 °C for ~96 h. All subsequent steps were performed at 4 °C unless stated otherwise. After harvesting, cells were washed in PBS and solubilized for 2–3 h in lysis buffer containing 50 mM Tris (pH 7.8), 250 mM NaCl, 0.7% (w/v) digitonin (Calbiochem), 0.3% (w/v) n-dodecyl-β-D-maltoside (Anatrace), 0.06% (w/v) cholesteryl hemisuccinate, and protease inhibitor mixture (Roche). The sample was then subjected to ultracentrifugation at 100,000 × g for 45 min to remove insoluble membranes and cell debris. The supernatant was incubated with Strep-Tactin resin (GE Healthcare) for 2 h, and the resin was washed with 20 column volumes of buffer A (50 mM Tris, pH 7.8, 250 mM NaCl, 0.08% digitonin). Protein was subsequently eluted with buffer A supplemented with 3.5 mM desthiobiotin. STEAP1-containing fractions (which exhibited a red color due to the presence of the heme cofactor) were concentrated to ~1.6 mg/ml with a 100-kDa-cutoff concentrator device (Amicon). Subsequently, 330 µl of STEAP1 was mixed with a large excess of Fab120.545 (145 µl at 9.7 mg/ml in PBS). After 1 h of incubation, the STEAP1-Fab mixture was injected onto a Superdex 200 increase 10/300 column (column volume, 24 ml; GE Healthcare) that had been preequilibrated in buffer containing 20 mM Tris (pH 7.8), 200 mM NaCl, and 0.08% (w/v) digitonin. Fractions containing the STEAP1-Fab complex were concentrated to a final concentration of ~5.0 mg/ml. Sample purity was assessed with SDS-PAGE analysis and analytical size-exclusion chromatography.

Grid preparation

Concentrated STEAP1-Fab120.545 (5.0 mg/ml) was incubated with 1 mM FAD on ice for 1 h before grid freezing. Then, 2.8 µl of sample was pipetted onto glow-discharged R1.2/1.3 Au holey carbon grids (200 mesh; Quantifoil) and plunge-frozen in a liquid ethane/propane mixture with a Vitrobot Mark IV (Thermo Fisher Scientific), blotting with force 0 for 4 s at 20 °C.

EM data collection

Movie collection was performed with a 200-kV Talos Arctica microscope (Thermo Fisher Scientific) equipped with a K2 summit detector (Gatan) and a postcolumn 20-eV energy filter. Using EPU (Thermo Fisher Scientific) in superresolution/counting mode (pixel size, 0.514 Å), movies were collected for 6.5 s in 26 frames with a dose of 1.905 e⁻/Å²/frame (measured in an empty hole without ice), corresponding to a total electron exposure of 49.5 e⁻/Å². Defocus values for collection in EPU were set between −1 and −3 μm but varied between −0.4 and −3.5 μm during data collection.

Image processing

A total of 5,352 movies were imported in the RELION v3.0 pipeline. The movies recorded in superresolution mode were binned at 2× (resulting pixel size, 1.03 Å) and motion corrected using UCSF MotionCor2 (37), followed by contrast transfer function (CTF) estimation using GCTF (38). A total of 695 movies were subsequently discarded, based on their poor CTF spectra, resulting in 4,657 movies (87% of total) for further processing; 1,791 particles were picked manually and 2D classified. The generated classes were used as templates for autopicking in RELION (39), resulting in 616,302 particles. The picked particles were 3D classified into six classes with no symmetry applied. The particles belonging to the class with most protein-like features (263,939 particles) were then subjected to CTF refinement and Bayesian polishing, followed by 3D classification without image alignment into three classes. The highest populated class (172,724 particles) showed clear amino acid side chain features. Particles were then CTF refined for a second time, and 431 junk particles were removed through 2D classifications. Automatic 3D refinement (with C3 symmetry applied) of the remaining 172,293 particles yielded a map at a global resolution of 3.8 Å, based on the gold-standard criterion of Fourier shell correlation (FSC) = 0.143. A postprocessing step in which the constant region of the Fab was masked out improved the resolution to 3.5 Å. Following the release of RELION v3.1beta with high-order aberration and anisotropic magnification estimation (40), we performed four additional rounds of CTF refinement and Bayesian polishing. This iterative process was followed by a 3D classification without image alignment into three classes, removing 2,867 particles. The final 169,426 particles were 3D autorefined (C3 symmetry) and subjected to a postprocessing step, improving the map resolution

to 3.0 Å (3.3 Å without masking), corresponding to ~1.44 times the Nyquist frequency.

Model building and refinement

To build the model for STEAP1, the TMD structure of human STEAP4 (residues 196–454) was rigid-body fitted into the cryo-EM map. For one chain, all STEAP4 residues were changed to the corresponding STEAP1 residue using the "mutate residue range" option in Coot (41), after which the model was manually inspected, adjusted, and refined in Coot. The model of this chain was copied and fitted in the density of the other two subunits. The starting model for the variable regions of Fab120.545 was obtained through the PIGS homology server (34) by uploading the heavy and light chain sequences. This model was rigid-body fitted in the cryo-EM map and the complementarity-determining regions were manually built in Coot. Then, the STEAP1-Fab120.545 model was iteratively refined using Coot (manually) and Phenix real-space refine (42) with geometric restraints and noncrystallographic symmetry constraints. Final refinements were performed using the non-sharpened cryo-EM map, in which the constant region of the Fab was masked out. The nonsharpened map revealed sufficient side chain detail for modelling. The final model uploaded to the PDB includes residues 67–312 of STEAP1, residues 1–112 of the Fab120.545 light chain, and residues 2–122 of the Fab120.545 heavy chain. Figures were prepared with Pymol (Schrödinger), UCSF Chimera (43), and UCSF ChimeraX (44).

Thermostability assays

Thermostability assays were performed as reported previously (29, 45, 46). Aliquots of purified STEAP1 (in 20 mM Tris, pH 7.8, 200 mM NaCl, 0.08% digitonin) were heated over a range of temperatures (20–75 °C) in a thermocycler for 10 min, cooled down, and centrifuged to remove aggregates. The supernatant was subsequently injected onto a Superdex 200 increase 10/300 column that had been equilibrated in buffer containing 20 mM Tris (pH 7.8), 200 mM NaCl, and 0.08% digitonin and was connected to a HPLC system (Shimadzu). The heme absorbance of STEAP1 was monitored at 412 nm using a SPD-20A UV-visible detector. In order to determine the melting temperature, peak maxima were normalized to the sample incubated at 20 °C and were fitted to a dose-response equation using GraphPad Prism 5.

Size-exclusion chromatography–binding assays with Fab variants

All Fab variants were diluted to a concentration of 0.5 mg/ml in PBS supplemented with 0.08% digitonin. Twenty-five microliters of purified STEAP1 (0.28 mg/ml in 20 mM Tris, pH 7.8, 200 mM NaCl, 0.08% digitonin) was mixed with 35 μl of PBS plus digitonin or a ~2-fold molar excess of Fab (35 μl at 0.5 mg/ml). After incubation for several hours, the mixtures were injected onto a Superdex 200 increase 3.2/300 column (column volume, 2.4 ml) that had been equilibrated in buffer containing 20 mM Tris (pH 7.8), 200 mM NaCl, and 0.08% digitonin and was connected to a HPLC system (Shimadzu). The heme absorbance of STEAP1 was monitored at 412 nm using a SPD-

20A UV-visible detector, whereas the tryptophan fluorescence (excitation at 275 nm and emission at 354 nm) emitted by both STEAP1 and Fab variants was detected using a RF-20Axs detector. STEAP1-Fab complex formation was assessed by comparing the peak elution profiles of mixtures with the profiles of individually injected proteins.

Ferric reductase assays

HEK293 GnTI⁻ suspension cells (U-Protein Express BV) were transfected with GFP-tagged STEAP constructs; ~96 h after transfection, cells were washed in PBS, resuspended in iron uptake buffer (25 mM MES, 25 mM MOPS, pH 7.0, 140 mM NaCl, 5.4 mM KCl, 1.8 mM $CaCl_2$, 0.8 mM $MgCl_2$, 5 mM glucose, 400 μM ferrozine), and pipetted into a 96-well plate (~5 × 10⁴ cells/well). Experiments were started by the addition of ferric citrate (Fisher Scientific) to each well (final concentration, 200 μM). The assay was performed in the dark at 37 °C for 35 min. Fe^{2+}-ferrozine formation was monitored using a model 680 microplate reader (Bio-Rad) at 550 nm. The Fe^{2+} formed was quantified using a standard curve that was generated as described (47). To assess the effect of Fab120.545 on the ferric reductase activity of the STEAP variants, cells were incubated with PBS or a range of Fab120.545 concentrations for 20 min prior to the addition of ferric citrate. Experiments were performed as technical triplicates by diluting cell stocks originating from single transfections three separate times. Error bars represent the S.D. Experiments in which activities were compared were carried out in parallel in the same 96-well plate. All statistical analyses were performed with GraphPad Prism 5.0. The ferric reductase activities of cells expressing different STEAP variants were compared for statistical significance using unpaired t tests, whereas paired t tests were employed to compare the same population of cells with or without the addition of Fab120.545.

Fluorescence microscopy

HEK293 GnTI⁻ suspension cells (U-Protein Express BV) were transfected with GFP-tagged STEAP constructs; ~96 h after transfection, cells were washed in PBS and then imaged for GFP (excitation at 488 nm and emission at 509 nm) using a CorrSight spinning disk confocal microscope (FEI), at a magnification of ×40, at 20 °C.

Data availability

Data supporting the findings of this manuscript are available from the corresponding authors upon reasonable request. The relevant cryo-EM density maps of the STEAP1-Fab120.545 complex have been deposited under accession number EMDB-10735. This deposition includes unfiltered half-maps, non-sharpened unmasked maps, and sharpened masked maps. Model coordinates of the structure have been deposited in the Protein Data Bank under accession number 6Y9B.

Abbreviations—The abbreviations used are: STEAP1, six-transmembrane epithelial antigen of the prostate 1; CTF, contrast transfer function; TMD, transmembrane domain; OxRD, oxidoreductase domain; RMSD, root mean square deviation; FSC, Fourier shell correlation.

References

1. Hubert, R. S., Vivanco, I., Chen, E., Rastegar, S., Leong, K., Mitchell, S. C., Madraswala, R., Zhou, Y., Kuo, J., Raitano, A. B., Jakobovits, A., Saffran, D. C., and Afar, D. E. (1999) STEAP: a prostate-specific cell-surface antigen highly expressed in human prostate tumors. *Proc. Natl. Acad. Sci. U.S.A.* **96**, 14523–14528 CrossRef Medline

2. Gomes, I. M., Maia, C. J., and Santos, C. R. (2012) STEAP proteins: from structure to applications in cancer therapy. *Mol. Cancer Res.* **10**, 573–587 CrossRef Medline

3. Moreaux, J., Kassambara, A., Hose, D., and Klein, B. (2012) STEAP1 is overexpressed in cancers: a promising therapeutic target. *Biochem. Biophys. Res. Commun.* **429**, 148–155 CrossRef Medline

4. Barroca-Ferreira, J., Pais, J. P., Santos, M. M., Goncalves, A. M., Gomes, I. M., Sousa, I., Rocha, S. M., Passarinha, L. A., and Maia, C. J. (2018) Targeting STEAP1 protein in human cancer: current trends and future challenges. *Curr. Cancer Drug Targets* **18**, 222–230 CrossRef Medline

5. Challita-Eid, P. M., Morrison, K., Etessami, S., An, Z., Morrison, K. J., Perez-Villar, J. J., Raitano, A. B., Jia, X. C., Gudas, J. M., Kanner, S. B., and Jakobovits, A. (2007) Monoclonal antibodies to six-transmembrane epithelial antigen of the prostate-1 inhibit intercellular communication in vitro and growth of human tumor xenografts in vivo. *Cancer Res.* **67**, 5798–5805 CrossRef Medline

6. Boswell, C. A., Mundo, E. E., Zhang, C., Bumbaca, D., Valle, N. R., Kozak, K. R., Fourie, A., Chuh, J., Koppada, N., Saad, O., Gill, H., Shen, B. Q., Rubinfeld, B., Tibbitts, J., Kaur, S., *et al.* (2011) Impact of drug conjugation on pharmacokinetics and tissue distribution of anti-STEAP1 antibody-drug conjugates in rats. *Bioconjug. Chem.* **22**, 1994–2004 CrossRef Medline

7. Sukumaran, S., Zhang, C., Leipold, D. D., Saad, O. M., Xu, K., Gadkar, K., Samineni, D., Wang, B., Milojic-Blair, M., Carrasco-Triguero, M., Rubinfeld, B., Fielder, P., Lin, K., and Ramanujan, S. (2017) Development and translational application of an integrated, mechanistic model of antibody-drug conjugate pharmacokinetics. *AAPS J.* **19**, 130–140 CrossRef Medline

8. Danila, D. C., Szmulewitz, R. Z., Vaishampayan, U., Higano, C. S., Baron, A. D., Gilbert, H. N., Brunstein, F., Milojic-Blair, M., Wang, B., Kabbarah, O., Mamounas, M., Fine, B. M., Maslyar, D. J., Ungewickell, A., and Scher, H. I. (2019) Phase I study of DSTP3086S, an antibody-drug conjugate targeting six-transmembrane epithelial antigen of prostate 1, in metastatic castration-resistant prostate cancer. *J. Clin. Oncol.* **37**, 3518–3527 CrossRef Medline

9. Doran, M. G., Watson, P. A., Cheal, S. M., Spratt, D. E., Wongvipat, J., Steckler, J. M., Carrasquillo, J. A., Evans, M. J., and Lewis, J. S. (2014) Annotating STEAP1 regulation in prostate cancer with [89]Zr immuno-PET. *J. Nucl. Med.* **55**, 2045–2049 CrossRef Medline

10. O'Donoghue, J. A., Danila, D. C., Pandit-Taskar, N., Beylergil, V., Cheal, S. M., Fleming, S. E., Fox, J. J., Ruan, S., Zanzonico, P. B., Ragupathi, G., Lyashchenko, S. K., Williams, S. P., Scher, H. I., Fine, B. M., Humm, J. L., *et al.* (2019) Pharmacokinetics and biodistribution of a [[89]Zr]Zr-DFO-MSTP2109A anti-STEAP1 antibody in metastatic castration-resistant prostate cancer patients. *Mol. Pharmacol.* **16**, 3083–3090 CrossRef Medline

11. Carrasquillo, J. A., Fine, B., Pandit-Taskar, N., Larson, S. M., Fleming, S., Fox, J. J., Cheal, S. M., O'Donoghue, J. A., Ruan, S., Ragupathi, G., Lyashchenko, S. K., Humm, J. L., Scher, H. I., Gonen, M., Williams, S., *et al.* (2019) Imaging patients with metastatic castration-resistant prostate cancer using [89]Zr-DFO-MSTP2109A anti-STEAP1 antibody. *J. Nucl. Med.* **60**, 1517–1523 CrossRef

12. Alves, P. M. S., Faure, O., Graff-Dubois, S., Cornet, S., Bolonakis, I., Gross, D. A., Miconnet, I., Chouaib, S., Fizazi, K., Soria, J. C., Lemonnier, F. A., and Kosmatopoulos, K. (2006) STEAP, a prostate tumor antigen, is a target of human CD8^{+} T cells. *Cancer Immunol. Immunother.* **55**, 1515–1523 CrossRef Medline

13. Schirmer, D., Grünewald, T. G. P., Klar, R., Schmidt, O., Wohlleber, D., Rubío, R. A., Uckert, W., Thiel, U., Bohne, F., Busch, D. H., Krackhardt, A. M., Burdach, S., and Richter, G. H. S. (2016) Transgenic antigen-specific, HLA-A*02:01-allo-restricted cytotoxic T cells recognize tumor-associated target antigen STEAP1 with high specificity. *Oncoimmunology* **5**, e1175795-11 CrossRef

14. Herrmann, V. L., Wieland, D. E., Legler, D. F., Wittmann, V., and Groettrup, M. (2016) The STEAP1262-270 peptide encapsulated into PLGA microspheres elicits strong cytotoxic T cell immunity in HLA-A*0201 transgenic mice: a new approach to immunotherapy against prostate carcinoma. *Prostate* **76**, 456–468 CrossRef Medline

15. Cappuccini, F., Stribbling, S., Pollock, E., Hill, A. V. S., and Redchenko, I. (2016) Immunogenicity and efficacy of the novel cancer vaccine based on simian adenovirus and MVA vectors alone and in combination with PD-1 mAb in a mouse model of prostate cancer. *Cancer Immunol. Immunother.* **65**, 701–713 CrossRef Medline

16. Chen, X., Wang, R., Chen, A., Wang, Y., Wang, Y., Zhou, J., and Cao, R. (2019) Inhibition of mouse RM-1 prostate cancer and B16F10 melanoma by the fusion protein of HSP65 & STEAP1186-193. *Biomed. Pharmacother.* **111**, 1124–1131 CrossRef Medline

17. Grunewald, T. G. P., Bach, H., Cossarizza, A., and Matsumoto, I. (2012) The STEAP protein family: versatile oxidoreductases and targets for cancer immunotherapy with overlapping and distinct cellular functions. *Biol. Cell* **104**, 641–657 CrossRef Medline

18. Ohgami, R. S., Campagna, D. R., Greer, E. L., Antiochos, B., McDonald, A., Chen, J., Sharp, J. J., Fujiwara, Y., Barker, J. E., and Fleming, M. D. (2005) Identification of a ferrireductase required for efficient transferrin-dependent iron uptake in erythroid cells. *Nat. Genet.* **37**, 1264–1269 CrossRef Medline

19. Ohgami, R. S., Campagna, D. R., McDonald, A., and Fleming, M. D. (2006) The Steap proteins are metalloreductases. *Blood* **108**, 1388–1394 CrossRef Medline

20. Korkmaz, K. S., Elbi, C., Korkmaz, C. G., Loda, M., Hager, G. L., and Saatcioglu, F. (2002) Molecular cloning and characterization of STAMP1, a highly prostate-specific six transmembrane protein that is overexpressed in prostate cancer. *J. Biol. Chem.* **277**, 36689–36696 CrossRef Medline

21. Korkmaz, C. G., Korkmaz, K. S., Kurys, P., Elbi, C., Wang, L., Klokk, T. I., Hammarstrom, C., Troen, G., Svindland, A., Hager, G. L., and Saatcioglu, F. (2005) Molecular cloning and characterization of STAMP2, an androgen-regulated six transmembrane protein that is overexpressed in prostate cancer. *Oncogene* **24**, 4934–4945 CrossRef Medline

22. Sikkeland, J., Sheng, X., Jin, Y., and Saatcioglu, F. (2016) STAMPing at the crossroads of normal physiology and disease states. *Mol. Cell. Endocrinol.* **425**, 26–36 CrossRef Medline

23. Whiteland, H., Spencer-Harty, S., Morgan, C., Kynaston, H., Thomas, D. H., Bose, P., Fenn, N., Lewis, P., Jenkins, S., and Doak, S. H. (2014) A role for STEAP2 in prostate cancer progression. *Clin. Exp. Metastasis* **31,** 909–920 CrossRef Medline

24. Isobe, T., Baba, E., Arita, S., Komoda, M., Tamura, S., Shirakawa, T., Ariyama, H., Takaishi, S., Kusaba, H., Ueki, T., and Akashi, K. (2011) Human STEAP3 maintains tumor growth under hypoferric condition. *Exp. Cell Res.* **317,** 2582–2591 CrossRef Medline

25. Jin, Y., Wang, L., Qu, S., Sheng, X., Kristian, A., Mælandsmo, G. M., Pällmann, N., Yuca, E., Tekedereli, I., Gorgulu, K., Alpay, N., Sood, A., Lopez-Berestein, G., Fazli, L., Rennie, P., *et al.* (2015) STAMP2 increases oxidative stress and is critical for prostate cancer. *EMBO Mol. Med.* **7,** 315–331 CrossRef Medline

26. Kleven, M. D., Dlakić, M., and Lawrence, C. M. (2015) Characterization of a single b-type heme, FAD, and metal binding sites in the transmembrane domain of six-transmembrane epithelial antigen of the prostate (STEAP) family proteins. *J. Biol. Chem.* **290,** 22558–22569 CrossRef Medline

27. Sendamarai, A. K., Ohgami, R. S., Fleming, M. D., and Lawrence, C. M. (2008) Structure of the membrane proximal oxidoreductase domain of human Steap3, the dominant ferrireductase of the erythroid transferrin cycle. *Proc. Natl. Acad. Sci. U.S.A.* **105,** 7410–7415 CrossRef Medline

28. Gauss, G. H., Kleven, M. D., Sendamarai, A. K., Fleming, M. D., and Lawrence, C. M. (2013) The crystal structure of six-transmembrane epithelial antigen of the prostate 4 (Steap4), a ferri/cuprireductase, suggests a novel interdomain flavin-binding site. *J. Biol. Chem.* **288,** 20668–20682 CrossRef Medline

29. Oosterheert, W., van Bezouwen, L. S., Rodenburg, R. N. P., Granneman, J., Förster, F., Mattevi, A., and Gros, P. (2018) Cryo-EM structures of human STEAP4 reveal mechanism of iron(III) reduction. *Nat. Commun.* **9,** 4337 CrossRef

30. Kim, K., Mitra, S., Wu, G., Berka, V., Song, J., Yu, Y., Poget, S., Wang, D.-N., Tsai, A.-L., and Zhou, M. (2016) Six-transmembrane epithelial antigen of prostate 1 (STEAP1) has a single *b* heme and is capable of reducing metal ion complexes and oxygen. *Biochemistry* **55,** 6673–6684 CrossRef Medline

31. Yamamoto, T., Tamura, Y., Kobayashi, J., Kamiguchi, K., Hirohashi, Y., Miyazaki, A., Torigoe, T., Asanuma, H., Hiratsuka, H., and Sato, N. (2013) Six-transmembrane epithelial antigen of the prostate-1 plays a role for in vivo tumor growth via intercellular communication. *Exp. Cell Res.* **319,** 2617–2626 CrossRef Medline

32. Genentech Inc. (February 18, 2015) Antibodies and immunoconjugates and uses therefor. U.S. Patent EP2502938B1

33. Scheres, S. H. W. (2012) RELION: implementation of a Bayesian approach to cryo-EM structure determination. *J. Struct. Biol.* **180,** 519–530 CrossRef Medline

34. Marcatili, P., Rosi, A., and Tramontano, A. (2008) PIGS : automatic prediction of antibody structures. *Bioinformatics* **24,** 1953–1954 CrossRef

35. Yang, Z. R., Thomson, R., McNeil, P., and Esnouf, R. M. (2005) RONN: the bio-basis function neural network technique applied to the detection of natively disordered regions in proteins. *Bioinformatics* **21,** 3369–3376 CrossRef Medline

36. Rougé, L., Chiang, N., Steffek, M., Kugel, C., Croll, T. I., Tam, C., Estevez, A., Arthur, C. P., Koth, C. M., Ciferri, C., Kraft, E., Payandeh, J., Nakamura, G., Koerber, J. T., and Rohou, A. (2020) Structure of CD20 in complex with the therapeutic monoclonal antibody rituximab. *Science* **367,** 1224–1230 CrossRef

37. Zheng, S. Q., Palovcak, E., Armache, J.-P., Verba, K. A., Cheng, Y., and Agard, D. A. (2017) MotionCor2: anisotropic correction of beam-induced motion for improved cryo-electron microscopy. *Nat. Methods* **14,** 332–333 CrossRef

38. Zhang, K. (2016) Gctf: real-time CTF determination and correction. *J. Struct. Biol.* **193,** 1–12 CrossRef Medline

39. Scheres, S. H. W. (2015) Semi-automated selection of cryo-EM particles in RELION-1.3. *J. Struct. Biol.* **189,** 114–122 CrossRef Medline

40. Zivanov, J., Nakane, T., and Scheres, S. H. W. (2020) Estimation of high-order aberrations and anisotropic magnification from cryo-EM data sets in RELION-3.1. *IUCrJ.* **7,** 253–267 CrossRef Medline

41. Emsley, P., and Cowtan, K. (2004) Coot: model-building tools for molecular graphics. *Acta Crystallogr. Sect. D Biol. Crystallogr.* **60,** 2126–2132 CrossRef

42. Adams, P. D., Grosse-Kunstleve, R. W., Hung, L.-W., Ioerger, T. R., McCoy, A. J., Moriarty, N. W., Read, R. J., Sacchettini, J. C., Sauter, N. K., and Terwilliger, T. C. (2002) PHENIX : building new software for automated crystallographic structure determination. *Acta Crystallogr. Sect. D Biol. Crystallogr.* **58,** 1948–1954 CrossRef

43. Goddard, T. D., Huang, C. C., and Ferrin, T. E. (2007) Visualizing density maps with UCSF Chimera. *J. Struct. Biol.* **157,** 281–287 CrossRef Medline

44. Goddard, T. D., Huang, C. C., Meng, E. C., Pettersen, E. F., Couch, G. S., Morris, J. H., and Ferrin, T. E. (2018) UCSF ChimeraX: meeting modern challenges in visualization and analysis. *Protein Sci.* **27,** 14–25 CrossRef Medline

45. Mancusso, R., Karpowich, N. K., Czyzewski, B. K., and Wang, D. N. (2011) Simple screening method for improving membrane protein thermostability. *Methods* **55,** 324–329 CrossRef Medline

46. Hattori, M., Hibbs, R. E., and Gouaux, E. (2012) A fluorescence-detection size-exclusion chromatography-based thermostability assay for membrane protein precrystallization screening. *Structure* **20,** 1293–1299 CrossRef Medline

47. Riemer, J., Hoepken, H. H., Czerwinska, H., Robinson, S. R., and Dringen, R. (2004) Colorimetric ferrozine-based assay for the quantitation of iron in cultured cells. *Anal. Biochem.* **331,** 370–375 CrossRef Medline